



# A Full-Spectrum Metal-Free Porphyrin Supramolecular Photocatalyst for Dual Functions of Highly Efficient Hydrogen and Oxygen Evolution

Zijian Zhang, Yongfa Zhu,\* Xianjie Chen, Hanjie Zhang, and Jun Wang

A full-spectrum (300–700 nm) responsive porphyrin supramolecular photocatalyst with a theoretical solar spectrum efficiency of 44.4% is successfully constructed. For the first time, hydrogen and oxygen evolution (40.8 and 36.1  $\mu\text{mol g}^{-1} \text{h}^{-1}$ ) is demonstrated by a porphyrin photocatalyst without the addition of any cocatalysts. The strong oxidizing performance also presents an efficient photodegradation activity that is more than ten times higher than that of  $\text{g-C}_3\text{N}_4$  for the photodegradation of phenol. The high photocatalytic reduction and oxidation activity arises from a strong built-in electric field due to molecular dipoles of electron-trapping groups and the nanocrystalline structure of the supramolecular photocatalyst. The appropriate band structure of the supramolecular photocatalyst adjusted via the highest occupied molecular orbital and lowest unoccupied molecular orbital energy levels of the porphyrin gives rise to thermodynamic driving potential for  $\text{H}_2$  and  $\text{O}_2$  evolution under visible light irradiation. Controlling the energy band structure of photocatalysts via the ordered assembly of structure-designed organic molecules could provide a novel approach for the design of organic photocatalysts in energy and environmental applications.

The energy band structure of a photocatalytic material plays a key role in determining the performances of photocatalyst. More specifically, the positions of the valence band (VB) and conduction band (CB) edges determine the redox ability, while the bandgap between them determines its spectral response.<sup>[1]</sup> The energy band structure is an intrinsic property of a given material and therefore difficult to adjust significantly. It has been shown previously that improving charge separation in photocatalysts is an effective strategy for improving their performance.<sup>[2]</sup> Therefore, based on these two key scientific issues, the development of nano-photocatalysts with proper energy band


and decent crystallization has become a research hotspot.<sup>[3]</sup> Research in this field has so far however mainly focused on inorganic materials.<sup>[4]</sup> Some of the limitations of inorganic photocatalysts include, but are not limited to, large bandgap energies that restrict the light absorption to the UV part of the solar spectrum;<sup>[5]</sup> complicated preparation methods;<sup>[6]</sup> or secondary pollution caused by toxic elements during the reaction.<sup>[7]</sup> In contrast, organic photocatalytic materials have some unique advantages. By designing molecular structures, it is possible to directly control the band positions of a semiconductor and therefore influence the ability to separate photogenerated charge carriers.<sup>[8]</sup> Besides, organic materials are rich in resources, safer, and more environmentally friendly. As a result, organic photocatalysts are attracting increasing interest from researchers. In particular, several organic dye molecules have been developed as

photocatalysts due to their large delocalization system and high spectrum efficiency.<sup>[9]</sup> Unfortunately, the performance of completely organic photocatalyst at present still does not match that of the inorganic materials. It might be caused by the poor separation and transportation of photogenerated carriers.

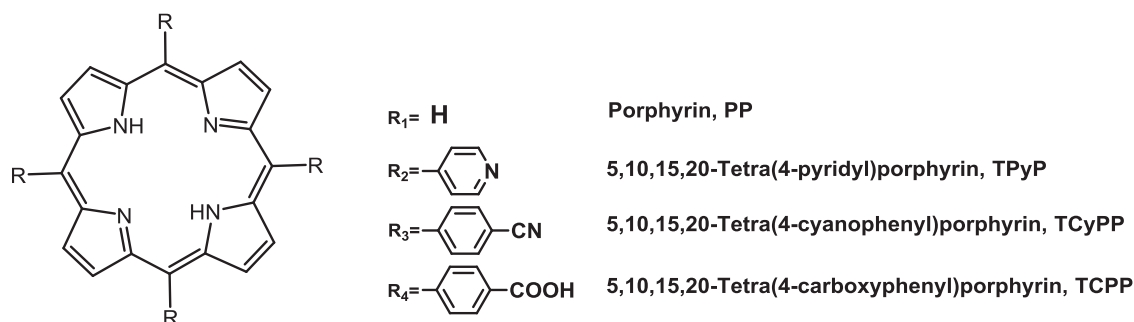
Porphyrin, a widely used molecule has recently captured our interest due to its excellence in photoelectric conversion.<sup>[10]</sup> From the porphyrin ring, a large number of modified derivatives are available, whose absorption spectrum covers the entire natural spectrum. Some materials based on porphyrin have also been reported for photocatalysis.<sup>[11]</sup> It should be pointed out however, that in most of those studies, porphyrin was used as a dye to broaden the spectral response range of another host material but did not as a photocatalyst itself.<sup>[12]</sup> In addition, the porphyrin-based photocatalysts employed for photocatalytic water splitting have so far only been able to drive the 2-electron half-reaction,<sup>[13]</sup> but not the 4-electron water oxidation. Furthermore, the hydrogen evolution reaction on porphyrin has typically required the assistance of noble metal cocatalysts. Given these limitation, the development of a noble metal-free porphyrin photocatalyst for water splitting is of significant scientific interest. Therefore, based on the above two fundamental scientific issues in photocatalysis, we aim to fabricate a porphyrin-host photocatalyst whose band structure and separation abilities of photogenerated carriers can be designed

Dr. Z. Zhang, Prof. Y. Zhu, Dr. X. Chen, Dr. H. Zhang, Dr. J. Wang  
Department of Chemistry  
Tsinghua University  
Beijing 100084, P. R. China  
E-mail: zhuyf@mail.tsinghua.edu.cn

Prof. Y. Zhu  
Anhui Provincial Key Laboratory for Degradation  
and Monitoring of Pollution of the Environment  
Fuyang Normal College  
Fuyang 236037, P. R. China

 The ORCID identification number(s) for the author(s) of this article can be found under <https://doi.org/10.1002/adma.201806626>.

DOI: 10.1002/adma.201806626



**Scheme 1.** Molecular structures of several porphyrin derivatives with different dipoles.

and well-regulated for water splitting in the absence of cocatalysts. All experimental details can be found in the Supporting Information.

Three porphyrin molecules with different substituents were successfully synthesized and characterized, as shown in **Scheme 1**. The differences in electronegativity of the substituents have a significant effect on the electron distributions and molecular dipoles of the respective porphyrin molecules. According to the calculated results, substituents with a higher electronegativity result in larger molecular dipoles as shown in **Figure 1a**. Tetra(4-carboxylphenyl)porphyrin (TCPP) presents the largest dipoles of 4.08 Debye among these derivatives, thereby creating a significant difference in potential between ring center and terminal substituents. Owing to the aggregation, the molecular isolated energy level was linearly combined into semiconductor energy band (Figure S1, Supporting Information) in self-assembled TCPP (SA-TCPP), which presented a single absorption edge of 700 nm indicating its ability of entire visible spectrum absorption, as shown in **Figure 1b**.

Moreover, the blueshift of the Soret band further improved the utilization of the UV spectrum by SA-TCPP. As a result, the theoretical spectral efficiency of SA-TCPP has been significantly improved to 44.4%, offering the possibility of full solar spectrum light harvesting. The photocurrent of SA-TCPP is as high as  $3.52 \mu\text{A cm}^{-2}$  compared to the untreated TCPP powder (Figure 1c), further indicating the directional movement of electrons and excellent separation of carriers in the material.

The self-assembled porphyrin photocatalysts presented efficient performances for water splitting as shown in **Figure 2a,b** and **Figure S2** in the Supporting Information. The SA-TCPP can efficiently decompose water into hydrogen at the rate of  $40.8 \mu\text{mol g}^{-1} \text{h}^{-1}$ , and into oxygen at the rate of  $36.1 \mu\text{mol g}^{-1} \text{h}^{-1}$ . The performances were compared to that of recently reported nonmetallic or porphyrin-based materials, which were listed in Table S1 in the Supporting Information. According to the comparison, most of those materials are limited to the hydrogen-producing half-reaction. And most of them require the assistance of cocatalysts to reduce

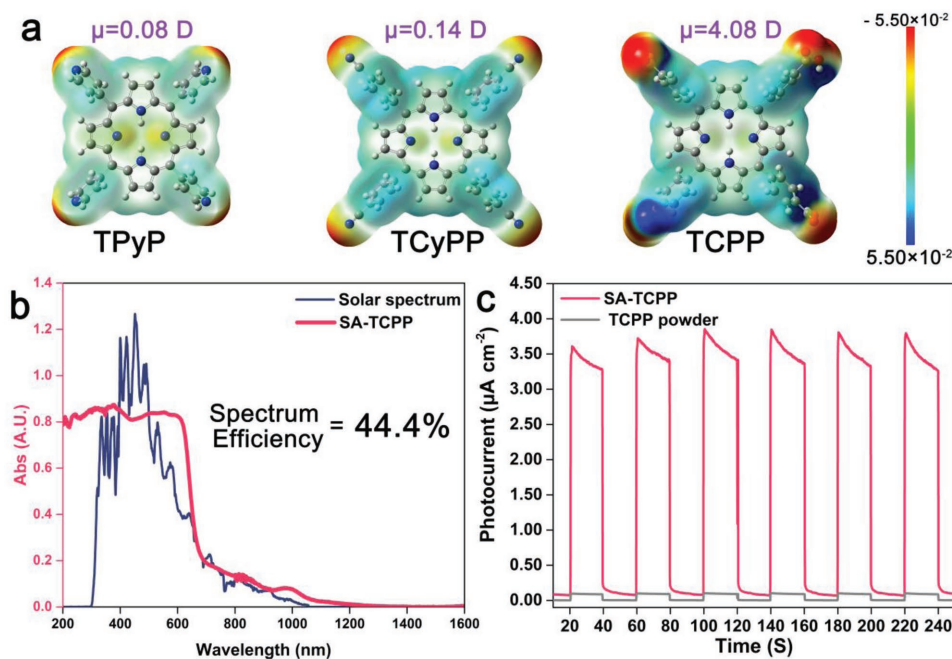


**Figure 1.** Electronic properties of TCPP. a) Diagram of molecular dipoles and electrons distribution in three porphyrin derivatives, unit of dipole moment: Debye. b) UV-vis diffuse reflection spectroscopy of SA-TCPP supramolecular photocatalyst, and solar spectrum observed by optical fiber spectrometer. c) Photocurrent response of SA-TCPP and untreated TCPP powder.

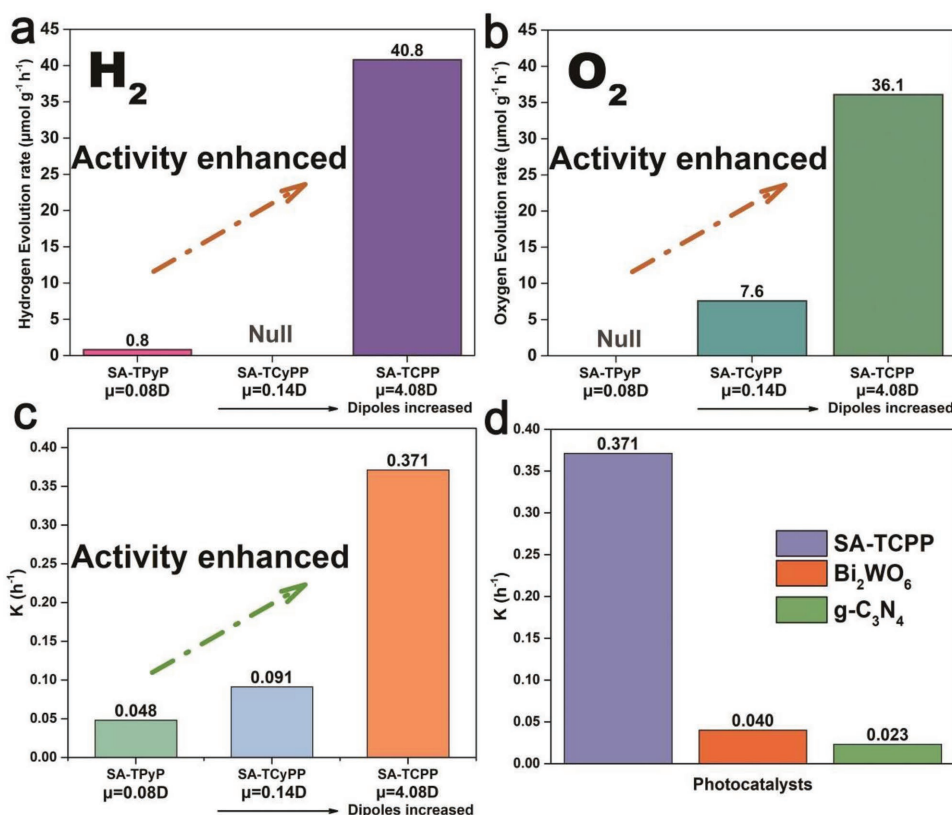


**Figure 2.** Enhanced photocatalytic activities with increased molecular dipoles. a) Photocatalytic hydrogen evolution without cocatalyst. b) Photocatalytic oxygen evolution without cocatalyst. c) Photocatalytic degradation for 2,4-DCP of 5.00 ppm. d) Comparison of apparent degradation rate constants  $k$  of different photocatalysts for 5.00 ppm 2,4-DCP, which is over ten times better than the inorganic  $\text{Bi}_2\text{WO}_6$  and  $\text{g-C}_3\text{N}_4$ .

the overpotential and activate the water molecules,<sup>[14]</sup> which undoubtedly consumes a large amount of precious metal resources. Therefore, we also compared and discussed the photocatalytic performances with Pt cocatalyst loaded as shown in Figure S3 in the Supporting Information, which did not significantly improve the hydrogen production performance of the photocatalysts. Thus, the cocatalyst-free SA-TCPP is capable of simultaneously achieving hydrogen and oxygen generation half-reactions, offering an environmentally friendly and resource-saving method for energy production.

Moreover, with such strong redox abilities, porphyrin supramolecular photocatalysts can efficiently degrade environmental pollutants as shown in Figure 2c. Compared with inorganic counterparts, the SA-TCPP was pointedly better than  $\text{g-C}_3\text{N}_4$  and  $\text{Bi}_2\text{WO}_6$ , as shown in Figure 2d and Figure S4 in the Supporting Information. The reaction rates were 15.8 times higher as that of  $\text{g-C}_3\text{N}_4$ <sup>[15]</sup> and 9.20 times as that of  $\text{Bi}_2\text{WO}_6$ .<sup>[16]</sup> Owing to the large conjugated system, aromatic pollutant molecules can be stalwartly adsorbed on the surface of SA-TCPP. These enriched pollutants were degraded swiftly into intermediate and mineralized products when the light turned on. The oxidizing degradation can be used for several phenolic contaminants. The apparent degradation rate constant  $k$  of 2,4-dichlorophenol (2,4-DCP), bisphenol A (BPA), and phenol is 0.371, 0.342, and 0.057  $\text{h}^{-1}$ , respectively. And the photocatalytic performances were significantly improved from partial visible spectrum to full spectrum as shown in Figure S5 in the

Supporting Information. Furthermore, the noncovalent SA-TCPP is stable and can be used for several times, as shown in Figures S6 and S7 in the Supporting Information.

Behind such excellent performances, it is important to explore the key scientific issues affecting the photocatalytic activity of the SA-TCPP supramolecular photocatalyst.

First, due to dipole-induced potential difference, a built-in electric field is formed in SA-TCPP.<sup>[17]</sup> The built-in electric field will be enhanced with the increase of the molecular dipole, accordingly promoting the separation of the photogenerated hole–electron pair.<sup>[18]</sup> As shown in Figure 2a–c, the photocatalytic activities are positively correlated with molecular dipoles. The dipole of the TCPP is the largest, reaching 4.08 Debye, thus the best photocatalytic performance of SA-TCPP. Further studies on improving the photocatalytic performance of organic photocatalysts by introducing groups with different electronic functions to adjust the molecular dipoles and thereby realizing better separation of photogenerated carriers will be summarized next.

Second, the SA-TCPP has its unique structural advantages. The four carboxylic groups of TCPP result in an excellent hydrophilicity (Figure S8, Supporting Information). Thus, the SA-TCPP has a better dispersibility in the aqueous phase system, which resulted in a greater reaction collision probability, so the reaction activity is better. More importantly, the SA-TCPP can be observed crystallized well with thin lamellar structure, the thickness of which is less than 25 nm as shown

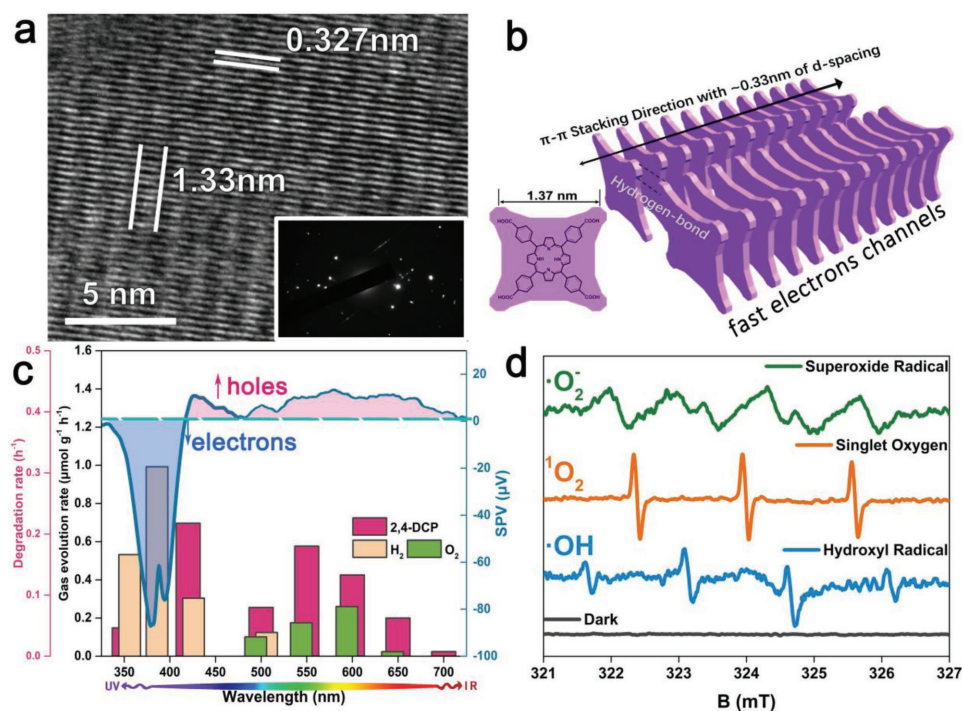


**Figure 3.** The highly crystalline structure of SA-TCPP and active species in the photocatalytic processes. a) HRTEM image of SA-TCPP and electron diffraction. b) The model of  $\pi$ - $\pi$  stacking of TCPP molecule from (a). c) Surface photovoltage spectrum (blue line), wavelength-dependent photocatalytic H<sub>2</sub> evolution, O<sub>2</sub> evolution, and 2,4-DCP degradation. d) Detection of superoxide radicals with 5,5-dimethyl-1-pyrroline N-oxide (DMPO) in MeOH, singlet oxygen with 2,2,6,6-tetramethylpiperidine (TEMP), and hydroxyl radicals with DMPO in H<sub>2</sub>O on ESR under light irradiation.

in Figure S9 in the Supporting Information. The diameters of SA-TCPP are distributed in the range of 10 nm (Figure S10, Supporting Information). It is well known that the mean free path of photogenerated carriers in organic materials is about 20 nm.<sup>[19]</sup> A regular crystal orientation and a crystallite of less than 20 nm can reduce the recombination of photogenerated electrons and holes. The microscopic crystal structure of the SA-TCPP was further investigated with the help of high-resolution transmission electron microscopy (HRTEM). The characteristic d-spacing of H-type  $\pi$ - $\pi$  stacking is 0.327 nm (Figure 3a),<sup>[20]</sup> which is equal to the distance between face-to-face TCPP molecules. Another 1.33 nm d-spacing is observed in the vertical direction, slightly smaller than the diameter of the TCPP molecule (about 1.37 nm), which is due to the molecule shrinkage from single molecular state to aggregated state.<sup>[21]</sup> Thus, fast-transporting channels of carriers in the  $\pi$ - $\pi$  stacking direction can be formed as shown in Figure 3b. Under the strong  $\pi$ - $\pi$  action, photogenerated carriers are produced as nonradiative transition due to aggregation-induced fluorescence quenching.<sup>[22]</sup> Transient fluorescence lifetime of SA-TCPP is 6.72 ns, which is much shorter than that of unassembled commercial TCPP powder (Figure S11 and Table S3, Supporting Information), demonstrating the more efficient transportation of photogenerated carriers in SA-TCPP.<sup>[22]</sup> As a result, the electric resistance of SA-TCPP is much smaller than that of nonassembled commercial TCPP powder as shown in Table S4 in the Supporting Information, which helps to improve quantum efficiency. Under illumination, the photogenerated carriers generated inside the material are separated by the built-in electric field, transmitted

through the  $\pi$ - $\pi$  channel, and reacted on the surface of the photocatalyst.

Third, the issue can be further understood from the perspective of molecular orbitals and electronic wave functions. According to the calculated molecular orbital map of TCPP in Figure S12 in the Supporting Information, the highest occupied molecular orbital (HOMO) and lowest unoccupied molecular orbital (LUMO) are mainly distributed in the delocalized electrons. It means the  $\pi$ - $\pi$  stacking mainly occurs in the frontier orbit of the electron transition, which leads to the overlap and combination of HOMO and LUMO, thereby the semiconductor band structure is constructed and the range of electron delocalization is further expanded. After that, whether the redox reaction is thermodynamically feasible depends mainly on the energy band positions. The calculation results proved that the introduction of substituents in the conjugated system significantly affected the frontier electron wave function of the molecule. As shown in Table S5 in the Supporting Information, as the electron-withdrawing effect of the substituents increases, the HOMO of derivatives decreases significantly, indicating that the oxidation ability of photogenerated holes is significantly strengthened. Thus, the photocatalytic oxidation ability of SA-TCPP is the strongest among these porphyrin supramolecular photocatalysts. Meanwhile, the forbidden band can be greatly reduced due to the expanded conjugation, which is manifested by a significant decrease in the CB bottom relative to the molecular LUMO energy level without an electron distribution. As shown in Figure S13 in the Supporting Information, the CB position of SA-TCPP was measured to be -0.24 eV (vs normal hydrogen electrode). Combined with the 700 nm absorption

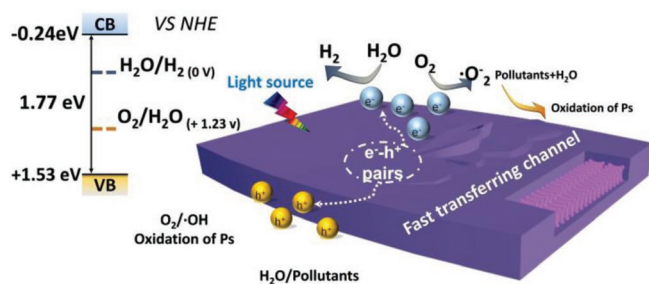


**Figure 4.** Schematic mechanism of the photocatalytic reactions by SA-TCPP.

edge in the UV–vis–NIR (near-infrared) spectrum, the energy gap of SA-TCPP is about 1.77 eV. As a result, the VB top position of SA-TCPP should be around +1.53 eV.

The main photogenerated carriers on the surface of photocatalyst can also be detected. For the SA-TCPP, in the Q band of 750–455 nm, it presents positive surface photovoltage (SPV) signal, indicating that photogenerated holes are the main carriers<sup>[23]</sup> and transferred to the surface to oxidize reactants ( $\text{H}_2\text{O}$  and pollutants). Following, when excited with higher energy in Soret band, the signal changes negatively and increases swiftly, demonstrating that the photo-induced valence electrons are injected into the CB,<sup>[23]</sup> which reacted with  $\text{H}_2\text{O}$  to produce hydrogen. Since unassembled TCPP powder does not have semiconductor-band structure, it cannot produce an obvious SPV signal. It is the property to generate holes and electrons at different wavelengths that SA-TCPP can produce both oxygen and hydrogen under the full spectrum. In addition, the wavelength-dependent reactions match with the SPV spectrum perfectly as shown in Figure 3c, signifying the different contributions of photogenerated carriers mentioned above. Besides, the other synergic intermediates (Figure 3d and Figure S14, Supporting Information), hydroxyl radicals, superoxide radicals, and singlet oxygen are uncovered by electron spin resonance (ESR) and radical captures. The reaction pathways were described by Equations (S1)–(S6) in the Supporting Information. From all the above, we suppose the mechanism of the photocatalytic process as the schematic model shown in Figure 4. First, the SA-TCPP with large built-in electric field is formed via  $\pi$ - $\pi$  stacking to get the fast-transporting channels of carriers. The proper energy bands result in excellent redox thermodynamic drive for water splitting and pollutants degradation. Under light irradiation, photogenerated carriers are separated by the built-in electric field and transferred to the surface of the photocatalyst through a crystallized delocalized system to react with different substrates.

In conclusion, a porphyrin supramolecular photocatalyst with theoretical solar spectrum efficiency of 44.4% was successfully constructed. It is the first time that hydrogen and oxygen evolutions were achieved by metal-free porphyrin photocatalyst without cocatalyst. The strong oxidation also presented an efficient photodegradation activity more than ten times higher than that of  $g\text{-C}_3\text{N}_4$ . It has been proved that the nanocrystal structure and built-in electric field due to molecular dipoles contribute to the excellent performances, which promote the separation of photogenerated carriers. The ability to produce hydrogen and oxygen is derived from the suitable supramolecular energy

band obtained by the proper HOMO and LUMO energy levels of porphyrin. Here, we describe a novel approach for the design of organic photocatalysts in energy and environmental applications based on conjugated dyes by molecular modification.

## Supporting Information

Supporting Information is available from the Wiley Online Library or from the author.

## Acknowledgements

This work was partly supported by Chinese National Science Foundation (21437003, 21673126, 21761142017, 21621003) and Collaborative Innovation Center for Regional Environmental Quality. The authors acknowledge the valuable comments and helpful revisions by Lukas Malms, Department of Materials, Imperial College London.

## Conflict of Interest

The authors declare no conflict of interest.

## Keywords

dipoles, dual functions, full spectrum, photocatalysis, supramolecular photocatalysts

Received: October 12, 2018

Revised: November 30, 2018

Published online:

- [1] C. E. Nebel, *Nat. Mater.* **2013**, *12*, 780.
- [2] a) J. Kou, C. Lu, J. Wang, Y. Chen, Z. Xu, R. S. Varma, *Chem. Rev.* **2017**, *117*, 1445; b) K. Mori, H. Yamashita, *Chem. - Eur. J.* **2016**, *22*, 11122.
- [3] C. S. Ponseca, P. Chabera, J. Uhlig, P. Persson, V. Sundstrom, *Chem. Rev.* **2017**, *117*, 10940.
- [4] a) Z. Song, B. Hong, X. Zhu, F. Zhang, S. Li, J. Ding, X. Jiang, J. Bao, C. Gao, S. Sun, *Appl. Catal., B* **2018**, *238*, 248; b) K. Wenderich, G. Mul, *Chem. Rev.* **2016**, *116*, 14587.
- [5] Y. Ma, X. L. Wang, Y. S. Jia, X. B. Chen, H. X. Han, C. Li, *Chem. Rev.* **2014**, *114*, 9987.
- [6] a) L. Liu, L. Ding, Y. Liu, W. An, S. Lin, Y. Liang, W. Cui, *Appl. Catal., B* **2017**, *201*, 92; b) C. Zhou, C. Lai, C. Zhang, G. Zeng, D. Huang, M. Cheng, L. Hu, W. Xiong, M. Chen, J. Wang, Y. Yang, L. Jiang, *Appl. Catal., B* **2018**, *238*, 6.
- [7] E. Friehs, Y. AlSalka, R. Jonczyk, A. Lavrentieva, A. Jochums, J.-G. Walter, F. Stahl, T. Scheper, D. Bahnemann, *J. Photochem. Photobiol., C* **2016**, *29*, 1.
- [8] P. M. Beaujuge, J. M. J. Frechet, *J. Am. Chem. Soc.* **2011**, *133*, 20009.
- [9] a) M. S. Eberhart, D. Wang, R. N. Sampaio, S. L. Marquard, B. Shan, M. K. Brennaman, G. J. Meyer, C. Dares, T. J. Meyer, *J. Am. Chem. Soc.* **2017**, *139*, 16248; b) Z. Zhang, J. Wang, D. Liu, W. Luo, M. Zhang, W. Jiang, Y. Zhu, *ACS Appl. Mater. Interfaces* **2016**, *8*, 30225; c) D. Liu, J. Wang, X. Bai, R. Zong, Y. Zhu, *Adv. Mater.* **2016**, *28*, 7284.

- [10] a) A. Mahmood, J.-Y. Hu, B. Xiao, A. Tang, X. Wang, E. Zhou, *J. Mater. Chem. A* **2018**, *6*, 16769; b) Ö. Birel, S. Nadeem, H. Duman, *J. Fluoresc.* **2017**, *27*, 1075; c) K. Liu, R. Xing, Q. Zou, G. Ma, H. Möhwald, X. Yan, *Angew. Chem., Int. Ed.* **2016**, *55*, 3036; d) C. Zhang, P. Chen, H. Dong, Y. Zhen, M. Liu, W. Hu, *Adv. Mater.* **2015**, *27*, 5379; e) X. Pan, L. Bai, H. Wang, Q. Wu, H. Wang, S. Liu, B. Xu, X. Shi, H. Liu, *Adv. Mater.* **2018**, *30*, 1800180.
- [11] a) Z. Liang, C. Qu, W. Guo, R. Zou, Q. Xu, *Adv. Mater.* **2018**, *30*, 1702891; b) T. He, S. Chen, B. Ni, Y. Gong, Z. Wu, L. Song, L. Gu, W. Hu, X. Wang, *Angew. Chem., Int. Ed.* **2018**, *57*, 3493.
- [12] a) P. K. Poddutoori, J. M. Thomsen, R. L. Milot, S. W. Sheehan, C. F. A. Negre, V. K. R. Garapati, C. A. Schmittenmaer, V. S. Batista, G. W. Brudvig, A. van der Est, *J. Mater. Chem. A* **2015**, *3*, 3868; b) F. Li, K. Fan, B. Xu, E. Gabrielsson, Q. Daniel, L. Li, L. Sun, *J. Am. Chem. Soc.* **2015**, *137*, 9153.
- [13] N. Zhang, L. Wang, H. M. Wang, R. H. Cao, J. F. Wang, F. Bai, H. Y. Fan, *Nano Lett.* **2018**, *18*, 560.
- [14] J. Yang, D. Wang, H. Han, C. Li, *Acc. Chem. Res.* **2013**, *46*, 1900.
- [15] M. Zhang, J. Xu, R. Zong, Y. Zhu, *Appl. Catal., B* **2014**, *147*, 229.
- [16] H. Fu, S. Zhang, T. Xu, Y. Zhu, J. Chen, *Environ. Sci. Technol.* **2008**, *42*, 2085.
- [17] a) L. Li, P. A. Salvador, G. S. Rohrer, *Nanoscale* **2014**, *6*, 24; b) Z. Z. Lou, P. Wang, B. B. Huang, Y. Dai, X. Y. Qin, X. Y. Zhang, Z. Y. Wang, Y. Y. Liu, *ChemPhotoChem* **2017**, *1*, 136.
- [18] a) M. Krzeszewski, E. M. Espinoza, C. Červinka, J. B. Derr, J. A. Clark, D. Borchardt, G. J. O. Beran, D. T. Gryko, V. I. Vullev, *Angew. Chem., Int. Ed.* **2018**, *57*, 12365; b) O. Cramariuc, P. J. Aittala, T. I. Hukka, *J. Mol. Model.* **2013**, *19*, 697.
- [19] T. K. Daubler, R. Bittner, K. Meerholz, V. Cimrova, D. Neher, *Phys. Rev. B* **2000**, *61*, 13515.
- [20] C. Janiak, *J. Chem. Soc., Dalton Trans.* **2000**, *21*, 3885.
- [21] S. Motoyama, R. Makiura, O. Sakata, H. Kitagawa, *J. Am. Chem. Soc.* **2011**, *133*, 5640.
- [22] N. C. Maiti, S. Mazumdar, N. Periasamy, *J. Phys. Chem. B* **1998**, *102*, 1528.
- [23] S. Li, D. Meng, L. Hou, D. Wang, T. Xie, *Appl. Surf. Sci.* **2016**, *371*, 164.